An Investigation into Aerodynamic Shape Optimization of Planar and Nonplanar Wings

David Koo[*] and David W. Zingg[†]

Centre for Research in Sustainable Aviation, Institute for Aerospace Studies, University of Toronto

4925 Dufferin St., Toronto, Ontario, M3H 5T6, Canada

Problems in three-dimensional aerodynamic shape optimization can produce complex design spaces due to the nonlinear physics of the Navier-Stokes equations and the large number of design variables used. In this paper, a Newton-Krylov optimization algorithm is applied to a set of complex aerodynamic optimization problems in order to investigate its behaviour and performance. The methodology solves the Reynolds-averaged Navier-Stokes equations with a parallel Newton-Krylov algorithm. Aerodynamic geometries are meshed using structured multi-block grids, which are then fitted with B-spline control volumes for mesh deformation and geometry control. A gradient-based optimization method is used, with adjoint variables calculated using a Krylov method. The optimization of the Common Research Model (CRM) wing is revisited, with a focus on the effect of varying geometric constraints and on the possibility of multimodality. In addition, several cases are presented which involve a high degree of shape change: two planform optimizations starting from a rectangular wing, and investigation of various wing tip treatments. The results characterize the methodology, demonstrating its robustness and ability to address optimization problems with substantial geometric freedom.

Nomenclature

α	Angle of attack
$\boldsymbol{\Lambda}$	Vector of adjoint variables
$\boldsymbol{\lambda}$	Mesh movement adjoint variables

---

[*] MASc Graduate

[†] University of Toronto Distinguished Professor in Computational Aerodynamics and Sustainable Aviation, Director, Centre for Research in Sustainable Aviation, Associate Fellow AIAA.

$\boldsymbol{\psi}$	Flow adjoint variables
$\boldsymbol{y}^+$	Non-dimensionalized wall distance
$\mathcal{G}$	Gradient vector
$\mathcal{J}$	Objective Function
$\mathcal{L}$	Lagrangian function
$\mathcal{M}$	Mesh movement residual
$\mathcal{R}$	Flow solution residual
$\mathbf{b}$	B-spline control point coordinates
$\mathbf{q}$	Flow variables
$\mathbf{v}$	Vector of design variables
$b/2$	Half-span
C_D	Coefficient of Drag
C_L	Coefficient of Lift
C_M	Coefficient of Moment
h/b	Tip height-to-span ratio
L/D	Lift-to-drag ratio
S_{ref}, S	Reference Area
S_{wet}	Wetted area
V	Volume
MAC	Mean Aerodynamic Chord

I. Introduction

The next generation of commercial transport aircraft will be designed with a heavy emphasis on fuel efficiency, with the goal of reducing operating costs and carbon dioxide emissions. The aviation industry has a goal, set by IATA, to reduce carbon emissions by 50% by the year 2050 relative to 2005 levels.[1,2] In order to meet this objective, engineering innovations will be required across multiple discplines, including propulsion, biofuels, aerodynamics, and structures. In the world of aerodynamics, advances in computing power and numerical optimization techniques have made computational fluid dynamics simulations a vital part of the design process, enabling engineers to make better design decisions.

Numerical aerodynamic shape optimization has seen rapid development in recent decades, enabled by the development of adjoint methods by Pironneau,[3] Angrand[4] and Jameson.[5] These methods enable one to efficiently compute the sensitivities of aerodynamic functionals such as lift and drag with respect to geometric design variables. These sensitivities in turn can be provided to gradient-based optimization methods to minimize a specified objective function. For convex design spaces, gradient-based methods provide a significant advantage in terms of convergence over gradient-free optimization algorithms, which scale poorly to higher dimensional problems.[6] At the same time, the increasing availability of large scale parallel computing has made it practical for aerodynamicists to solve complex flows and to utilize optimization algorithms requiring many such flow evaluations.

While aerodynamic optimization was first applied to inviscid two-dimensional cases, the types of problems grew in complexity as the algorithms matured. For example, Jameson and Reuther[7] applied a continuous adjoint method using the Euler equations to optimize airfoils on structured grids. Later, researchers such as Anderson and Bonhaus[8] or Nemec et al.[9] focused on incoporating turbulence models into airfoil optimization. Three-dimensional optimizations soon followed - examples include the work of Elliot and Peraire[10] with the Euler equations, and Nielsen and Anderson[11] who implemented the Spalart-Allamaras turbulence model on unstructured grids.

Current state-of-the-art codes use the Reynolds-Averaged Navier-Stokes (RANS) equations on three-dimensional wings and even full aircraft configurations. Examples of such methods include SYN107 developed by Jameson[12] and *elsA* developed by ONERA.[13] OPTIMAS, developed by Peigin and Epstein,[14,15] is an example of aerodynamic optimization method powered by a genetic algorithm. Further examples of current aerodynamic shape optimization methodologies can be found in Refs. 13, 16–23.

While efforts in the aerodynamic community have focused on making incremental changes in wing shape, the aggressive targets for reducing carbon emissions set by the aviation industry suggest that more a flexible tool is needed, one that can deal with larger design spaces and guide engineers in making early design decisions based on high-fidelity analysis. Such a tool can be used to optimize and compare unconventional configurations such as the blended-wing-body, box wing, strut-braced wing, or double-bubble configurations.[24–26]

When incorporating larger shape changes, aerodynamic shape optimization has often been performed using lower fidelity models. For example, Jansen and Martins[27] used a panel method to compute induced drag for nonplanar lifting surfaces and used drag polar data to predict viscous drag; Ning and Kroo[28] used a vortex-lattice method for computing induced drag and assumed a parabolic relationship between viscous drag and lift in their numerical study on winglets; Hicken and Zingg[29,30] applied an Euler-based optimization to nonplanar wing geometries.

As the design space expands, the notion of multimodality, the existence of multiple locally optimum solutions, becomes relevant. Gradient-based methods offer the advantage of fast convergence to an optimum; however they may arrive at local minima. While stochastic methods are capable of locating global optima, they converge slowly as the number of design variables increases.[6,31] In their study on multimodality, Chernukhin and Zingg[32] demonstrated the viability of a gradient-based multi-start method for global optimization.

This paper makes use of Jetstream, a high fidelity solver and gradient-based aerodynamic shape optimization methodology developed for the Euler equations by Hicken and Zingg,[29] and extended to the RANS equations by Osusky et al.[33] Among other cases, Osusky et al. applied the method to optimize the airfoil sections of the Common Research Model (CRM) wing geometry, a case that subsequently became one of the benchmark problems for the Aerodynamic Design Optimization Discussion Group (ADODG).[23] In their studies of the CRM wing, optimizations with variations of the initial geometry converged to different optimal geometries but with similar drag counts. As a result, they suggested the existence of either a multimodal or flat design space. Osusky et al. also applied Jetstream to design an optimal planform for a rectangular NACA 0012 wing and were successful in showing the code's ability to produce large scale planform changes when accounting for viscous and turbulent effects. Despite this, their optimization produced less than optimal planform designs, due to difficulties morphing the mesh and obtaining converged flow solutions.

Building upon the contributions by Osusky et al.,[33] this paper aims to demonstrate Jetstream as a methodology capable of aerodynamic optimization in large design spaces, beginning with a follow-up on the CRM wing section optimization, looking at both multimodality and how the results vary depending on geometric constraints. Following this, Jetstream will be applied to two cases with a much higher level of geometric freedom: the first case revisits the planform optimization problem studied by Osusky et al., and the second is a nonplanar wingtip optimization which follows up on the work of Hicken and Zingg,[29] this time using the RANS equations. The latter two case studies will make use of improvements to Jetstream's geometric flexibility developed by Gagnon and Zingg,[25] which are outlined in Section II. The remainder of this paper is divided as follows: Section II provides a brief overview of the theoretical background behind Jetstream, followed by Section III where the optimization results of the aforementioned cases are presented.

II. Methodology

A brief summary of the methodology behind Jetstream is presented here. A more detailed description can be found in Osusky et al.[33] and Hicken and Zingg.[29] The methodology can be broken down into five major components: geometry parameterization and control, mesh deformation, flow solver, gradient evaluation, and the optimization algorithm.

A. Geometry Parameterization, Control, and Mesh Deformation

Before optimization, the initial computational mesh is fitted to a B-spline control volume,[34] as shown in the left and middle parts of Figure 1. The control volume defines a mapping to the physical space $P \subset \mathbb{R}^3$ from parametric coordinate space $D = \boldsymbol{\xi} = (\xi, \eta, \zeta) \in \mathbb{R}^3 | \xi, \eta, \zeta \in [0, 1]$. To fit the initial computational mesh, $\boldsymbol{\xi}$ values for each node are calculated using a chord-length parameterization along grid lines. Spatially varying knot vectors are computed, and a least-squares problem is solved to determine B-spline control point coordinates that create the best fit to the initial grid. Further details regarding the knot vectors and the fitting process can be found in Ref. 29. The number of control points is user-defined and is typically around 5-9 points in each direction, in order ensure a good fit for the grid.

The control points defining the aerodynamic geometry form a B-spline surface and are manipulated by the optimizer. Once the geometry has been modified, the B-spline volume control mesh is deformed using a linear-elasticity model to propagate displacements on the B-spline surface to the rest of the control volume.[35] In practice, the mesh deformation is split into m linear increments:

$$\mathbf{K}^{(i)}(\mathbf{b}^{(i)} - \mathbf{b}^{(i-1)}) - \mathbf{f}^{(i)} = 0 \quad \text{for } i = 1....m, \tag{1}$$

where $\mathbf{K}^{(i)}$ is the symmetric positive-definite stiffness matrix computed at each increment, $\mathbf{b}^{(i)}$ is the vector of control point locations at each increment, and $\mathbf{f}^{(i)}$ is the discrete forcing vector defined by the displacements at the surface. The mesh movement equations are solved using the conjugate gradient method preconditioned with ILU(p).[36] The B-spline volume control mesh usually has fewer than 10^3 nodes per block, so the mesh movement equations are solved relatively quickly while mesh quality is maintained. Once the new control point locations are computed, the grid is recomputed algebraically based on the B-spline mapping and the parametric coordinates of the grid nodes.

When the wing optimization problem is limited to designing the twist and section airfoil shape, it is sufficient to supply the z-coordinates of the wing surface B-spline points as variables for the optimizer. While it is intuitive and simple to set up, this surface-based geometry control method requires a number of linear constraints to prevent intersecting surfaces. These constraints will vary depending on the grid topology. To improve optimization performance, the z-coordinates of the B-spline control points are usually scaled so that they are on the order of 10^{-1} to 10^0.

Volume-based geometry control, borrowed from the animation industry,[37] provides a more robust and intuitive way to parameterize both large scale design variables as well as section design variables. This feature was implemented into Jetstream by Gagnon and Zingg,[38] and addresses the shortcomings of the direct surface-based geometry control. A new set of points are introduced as design variables, known as the

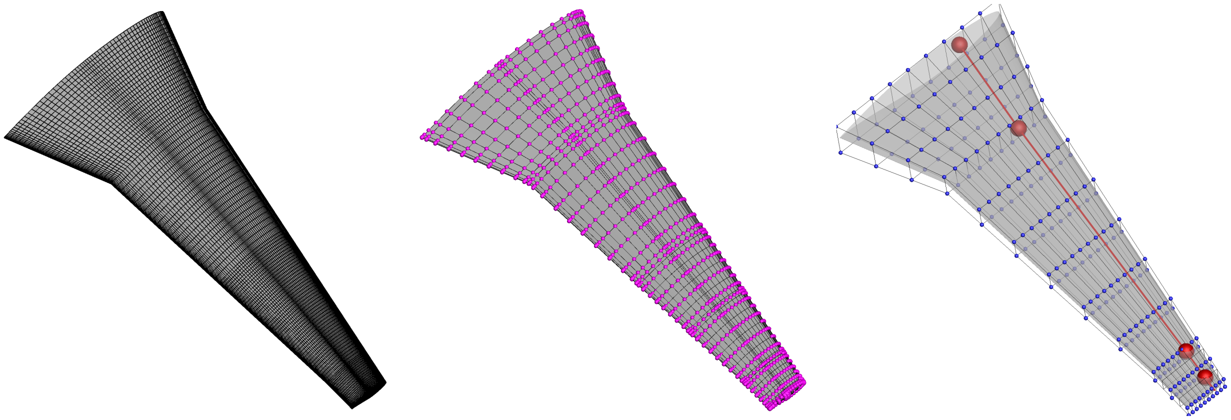

Figure 1: The CFD mesh (left) is approximated with a B-spline control mesh (middle). The points of this B-spline control mesh, shown in magenta, are used to deform the mesh and can also be design variables. For more complex optimizations, the B-spline surface is embedded into an FFD volume (right). The FFD lattice points are shown in blue and the axial curve and its points are shown in red.

Free-Form Deformation (FFD) volume, shown on the right side of Figure 1. The B-spline surface points on the aerodynamic geometry are embedded inside the FFD volume, which can have any number of user-defined control points. As the FFD volume deforms, the embedded wing surface deforms accordingly, while maintaining its continuity and smoothness. Each FFD volume is also associated with an axial curve, which can be thought of as the driving curve of the wing, controlling its span, sweep, and dihedral. The axial curve itself is a non-uniform rational B-spline (NURBS) curve defined by another set of control points.

When the axial curve control point coordinates are included as design variables, the optimizer can design the planform with fewer linear constraints. The axial curve can be defined as a polynomial curve of any order. For control of airfoil shape, twist, and chord, design variables are specified as the coordinates of the FFD lattice points along their local x and z-axes orthogonal to the axial curve. Additionally, FFD point coordinates are scaled so that they are approximately the same order of magnitude as axial curve control points. It is important to stress that changes in the FFD shape apply to the B-spline control points, not directly to nodes of the computational mesh. Mesh movement is a two-step process,[35] with the linear elasticity equations applied to the B-spline volume control mesh. This way, analytical representation of the geometry is preserved. The sensitivity of the aerodynamic surface has an exact mapping to the sensitivity with respect to the FFD control points, a property which is vital to gradient computation.

B. Flow Solver

Jetstream is based on a parallel, implicit, multi-block structured finite-difference solver which solves the RANS equations[39] with the Spalart-Allmaras one-equation turbulence model. Spatial discretization of the governing equations is performed using second-order summation-by-parts operators. Boundary and block interface conditions are enforced weakly through simultaneous approximation terms.[40] An inexact Newton approach is used to solve the discretized steady RANS equations, represented here by

$$\boldsymbol{\mathcal{R}}(\mathbf{q}) = 0, \tag{2}$$

where $\boldsymbol{\mathcal{R}}$ is the flow solution residual and $\mathbf{q}$ is the vector of flow variables. If the initial solution $\mathbf{q}^{(0)}$ is sufficiently close to the converged solution, Newton's method will converge quadratically. Thus, the solution method is split into two phases, the first using implicit Euler time marching to compute an initial iterate. Once the flow residual is reduced by several orders of magnitude, this solution is then used to initiate the inexact-Newton phase.

During both stages of the solver, the flexible generalized minimal residual (GMRES) method with an approximate-Schur parallel preconditioner is employed to solve the linear system at each iteration. A scalar artificial dissipation scheme[41, 42] is used for the cases in this paper, but matrix dissipation[43] can also be used. This flow solver methodology was validated using the NASA Common Grid study from the Fifth Drag Prediction Workshop (DPW5), producing a grid-converged drag coefficient that was within one drag count of the median value obtained by all the participants.[39, 44]

C. Gradient Evaluation

The gradients of the aerodynamic functionals are computed using the discrete-adjoint method, which is briefly summarized here. The optimization problem is first formulated to include the flow and mesh movement constraints:

$$\begin{aligned}
&min && \mathcal{J}(\mathbf{v},\mathbf{q},\mathbf{b}^{(m)}), && \text{(3a)}\\
&s.t. && \boldsymbol{\mathcal{M}}^{(i)}(\mathbf{v},\mathbf{b}^{(i)},\mathbf{b}^{(i-1)}) = 0, \quad i = 1,2,...,m && \text{(3b)}\\
& && \boldsymbol{\mathcal{R}}(\mathbf{v},\mathbf{q},\mathbf{b}^{(m)}) = 0, && \text{(3c)}
\end{aligned}$$

plus geometric and flow-dependent constraints, where $\mathcal{J}$ is the objective function, $\mathbf{v}$ are the design variables, $\mathbf{q}$ are the flow variables, and $\mathbf{b}^{(m)}$ are the B-spline volume control points. The m mesh movement equations are written here as $\boldsymbol{\mathcal{M}}^{(i)}$, which are solved for $\mathbf{b}^{(i)}$, the B-spline volume control-points at the ith increment. The flow residual is rewritten here to include the design variables and the B-spline volume control points. The Lagrangian function is introduced:

$$\mathcal{L}(\mathbf{v},\mathbf{q},\{\mathbf{b}^{(i)},\boldsymbol{\lambda}^{(i)}\}_{i=1}^{m},\boldsymbol{\psi}) = \mathcal{J}(\mathbf{v},\mathbf{q},\mathbf{b}^{(m)}) + \sum_{i=1}^{m}\left(\boldsymbol{\lambda}^{(i)^T}\boldsymbol{\mathcal{M}}^{(i)}(\mathbf{v},\mathbf{b}^{(i)},\mathbf{b}^{(i-1)})\right) + \boldsymbol{\psi}^T\boldsymbol{\mathcal{R}}(\mathbf{v},\mathbf{q},\mathbf{b}^{(m)}), \tag{4}$$

where $\{\boldsymbol{\lambda}^{(i)}\}_{i=1}^{m}$ are the mesh adjoint variables, and $\boldsymbol{\psi}$ is the vector of flow adjoint variables. The Karush-Kuhn-Tucker (KKT) first-order optimality conditions are obtained by setting the partial derivatives of $\mathcal{L}$ with respect to each of its arguments to zero.[29, 35, 45] Setting $\partial\mathcal{L}/\partial\boldsymbol{\lambda}^{(i)}$ gives the mesh movement equations for increment i, while setting $\partial\mathcal{L}/\partial\boldsymbol{\psi} = 0$ returns the flow equations. Setting $\partial\mathcal{L}/\partial\mathbf{q} = 0$ gives the flow adjoint system,

$$\left(\frac{\partial\boldsymbol{\mathcal{R}}}{\partial\mathbf{q}}\right)^{T}\boldsymbol{\psi} = -\left(\frac{\partial\mathcal{J}}{\partial\mathbf{q}}\right)^{T}. \tag{5}$$

Setting $\partial\mathcal{L}/\partial\mathbf{b}^{(i)} = 0$ leads to the mesh adjoint equations,

$$\left(\frac{\partial\boldsymbol{\mathcal{M}}^{(m)}}{\partial\mathbf{b}^{(m)}}\right)^{T}\boldsymbol{\lambda}^{(m)} = -\left(\frac{\partial\boldsymbol{\mathcal{J}}}{\partial\mathbf{b}^{(m)}}\right)^{T} - \left(\frac{\partial\boldsymbol{\mathcal{R}}}{\partial\mathbf{b}^{(m)}}\right)^{T}\boldsymbol{\psi} \tag{6}$$

for the last mesh movement increment, and

$$\left(\frac{\partial\boldsymbol{\mathcal{M}}^{(i)}}{\partial\mathbf{b}^{(i)}}\right)^{T}\boldsymbol{\lambda}^{(i)} = -\left(\frac{\partial\boldsymbol{\mathcal{M}}^{(i+1)}}{\partial\mathbf{b}^{(i)}}\right)^{T}\boldsymbol{\lambda}^{(i+1)} \quad \text{for } i = m-1 \ldots 1 \tag{7}$$

for each preceding increment. At each iteration of the optimization algorithm, after a new set of design variable values is calculated by the optimization algorithm, the mesh is first updated and the flow evaluated. The adjoint variables $\boldsymbol{\psi}$ and $\boldsymbol{\lambda}^{(i)}$ are then obtained by solving Equation (5) first, followed by (6), and finally (7). The flow adjoint system is solved using GCROT(m,k), a flexible and simplified version of the GCROT method,[46] to a residual tolerance of 10^{-8}. The matrix on the left hand side of the mesh adjoint system is symmetric positive definite and the systems are solved using the preconditioned conjugate gradient method.[29] Once the adjoint variables are known, taking the derivative $\partial\mathcal{L}/\partial\mathbf{v}$ leads to the gradient with respect to the design variables:

$$\frac{d\mathcal{L}}{d\mathbf{v}} = \frac{\partial\mathcal{J}}{\partial\mathbf{v}} + \sum_{i=1}^{m}\boldsymbol{\lambda}^{(i)T}\frac{\partial\boldsymbol{\mathcal{M}}^{(i)}}{\partial\mathbf{v}} + \boldsymbol{\psi}^{T}\frac{\partial\boldsymbol{\mathcal{R}}}{\partial\mathbf{v}}, \tag{8}$$

which is then passed to the optimization algorithm.

D. Optimization Algorithm

Since Equation (8) yields the total derivative, the optimization problem can now be posed as minimizing $\mathcal{J}$, solely with respect to user-specified design variables $\mathbf{v}$, and any additional geometric or force constraints. To solve this optimization problem, Jetstream uses SNOPT (Sparse Nonlinear OPTimizer),[47] a sparse SQP method, to provide updated design variables. For aerodynamic optimization, an adjoint solution at each iteration is required for the objective function, drag, as well as for any flow solution dependent constraints. Geometric constraints such as wing thickness are formulated as linear relationships between design variables,

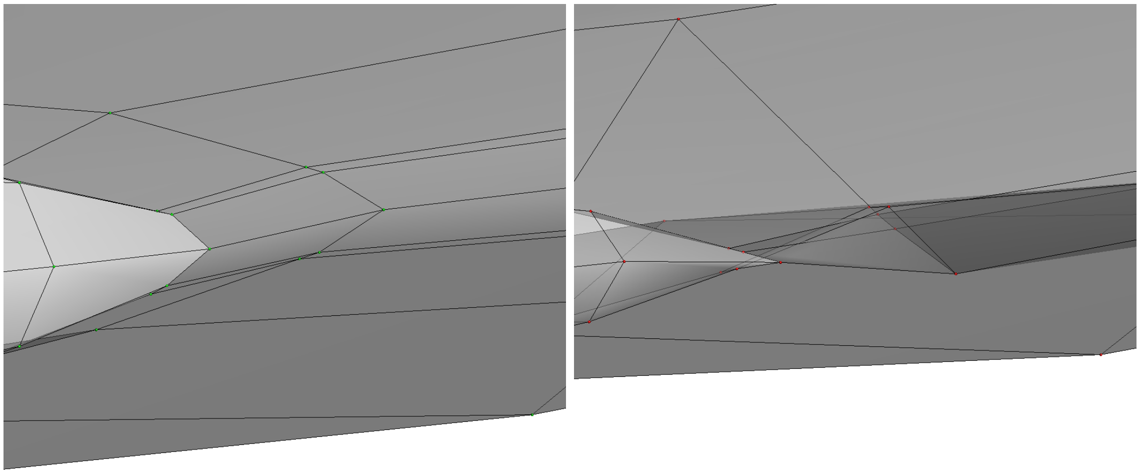

(a) Initial B-spline mesh at the wingtip

(b) Deformed B-spline mesh

Figure 2: B-spline surface crossover in the CRM wing optimization at the leading edge near wingtip

which SNOPT satisfies exactly. Finally, complex geometric constraints such as wing volume or projected area are provided as nonlinear constraints, along with their respective gradients.

III. Results

In the work of Osusky et al.,[33] the results did not converge fully to the optimal solution, often reducing the gradient of the Lagrangian (including all constraints - this is known as “optimality”) by less than an order of magnitude. Upon further investigation, these issues were found to be related to a tendency to collapse the leading edge and create self-intersecting surfaces. These surfaces resulted in meshes that were either invalid or of poor quality, creating problems for the flow solver and eventually causing the optimization to stall. As shown in Figure 2, these issues stem from applying a surface-based parameterization to the leading edge of a wing with an O-grid topology. To address this issue, an additional set of linear constraints was created on the z-coordinates of the leading edge control points to prevent the resulting surfaces from intersecting or becoming infinitely thin. This change resulted in better flow solver and optimizer performance, leading to deeper convergence. In the planform and winglet optimization cases later on, surface intersection issues are avoided altogether by using FFD-based geometry control. This approach decouples the geometry control from the B-spline surface parameterization.[38,48]

A. CRM Wing Section Optimization: Thickness Constraints

In the benchmark optimization problem posed to the ADODG, the wing is extracted from the NASA CRM wing-body geometry and the objective is to minimize C_D by optimizing the section shape and twist at any number of spanwise sections. The wing geometry, reference area, and reference point are all non-

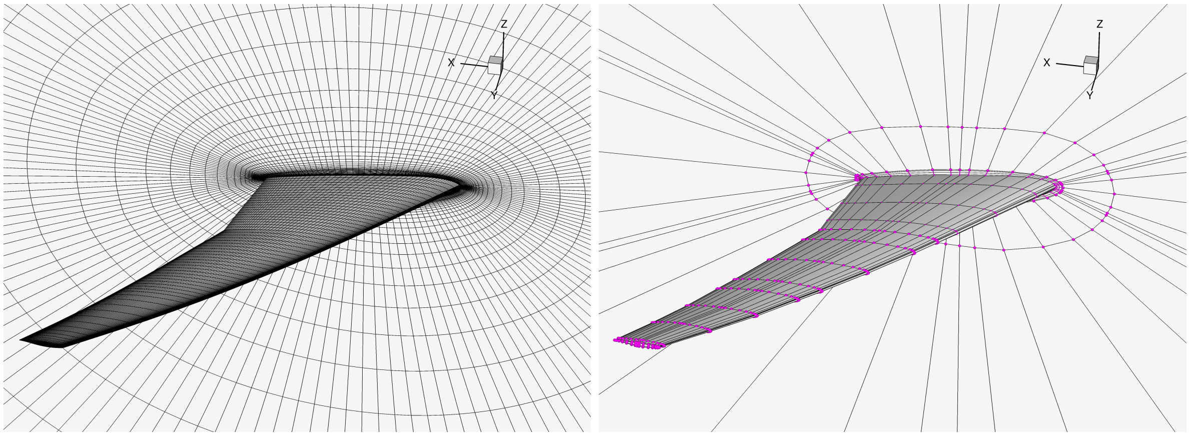

(a) CFD Mesh (b) B-spline Surface

Figure 3: The computational mesh and B-spline surface for the CRM wing geometry. The wing is controlled by the coordinates of the B-spline control points (magenta)

dimensionalized by the mean aerodynamic chord, 275.8 inches. The wing is optimized at a Mach number of 0.85 and Reynolds number of 5 million. The following constraints are imposed on the optimization problem:

- a lift coefficient constraint, $C_L = 0.50$;
- a pitching moment constraint, $C_M \geq -0.17$ about the y-axis centered at (1.2077, 0, 0.007669) in reference units;
- the wing projected area is constant, $S_{\text{ref}} = 3.407$ squared reference units;
- a minimum volume constraint equal to its original volume, $V = 0.2617$ cubed reference units;
- a minimum thickness constraint at every section, equal to 25% of the original thickness.

Figure 3 shows the computational grid as well as the fitted B-spline surface. The B-spline surface has 15 spanwise design sections, each with 17 chordwise control points on the upper and lower surfaces. The z-coordinates of the B-spline surface points are the design variables, while the trailing edge is fixed. The root twist is fixed, and the angle of attack is free. Table 1 shows the information on the two grid levels used, with the 'Coarse' level being used for optimization. Lift and drag coefficients for both the baseline and optimized geometries are computed on the 'Fine' mesh level, which results in computed drag coefficients within 1% of the grid-converged values.[39,49]

While the optimizer is constrained to maintain the initial wing volume, results from the AIAA SciTech conferences[49–51] have shown that some optimization methods, including Jetstream, can exploit the 25% minimum thickness, designing outboard wing sections that are unrealistically thin. In these results, the original volume is redistributed by thickening the wing sections near the root. Some groups presented a variation on the problem allowing no thickness reduction.[52,53] This result raises the question of how the design space is affected by changing the wing thickness requirements, and how much of the drag reduction

Table 1: Grid parameters for CRM wing grid study

Grid	**Nodes**	**Blocks**	**Off-wall Spacing** (ref. units)	y^+
Coarse	925,888	40	1.5×10^{-6}	0.33
Fine	7,407,104	320	8.1×10^{-7}	0.17

Table 2: Results for CRM wing single-point optimization with different thicknesses, evaluated on the Fine mesh

	C_D (counts)	C_M
Baseline	201.5	-0.1747
25% minimum thickness	185.2	-0.1702
75% minimum thickness	186.7	-0.1708
100% minimum thickness	191.0	-0.1725

results from the unusually thin wing sections. To investigate the impact of thickness constraints, the CRM wing optimization was performed with both a 75% minimum thickness constraint and a 100% minimum thickness constraint, in addition to the 25% constraint.

Table 2 shows the drag counts of the various optimized geometries. Figure 4 shows the various optimized geometries and pressure distributions. All of the optimizations are able to reduce the drag and remove the shock near the root, while the outboard sections show the most variation in pressure distribution between the runs. The thickening of the root section is reduced as the thickness constraint increases, due to the optimizer's inability to redistribute the wing volume.

The optimized geometry at 25% thickness has the lowest drag coefficient, as expected. However, there is a difference of only 1.5 drag counts between optimized result at 75% thickness and 25% thickness, meaning that most of the drag reduction results from subtle changes in the section shape and twist, while the thin outboard wing sections provide a relatively small benefit. When the optimizer is prevented from making any thickness reductions, the difference in drag coefficient is greater, at 5 counts. With the 100% minimum thickness constraint, the optimizer is extremely restricted in its ability to contour the airfoil since the vertical distance between every pair of upper and lower control point cannot decrease. Although ultimately wing thickness is determined by structural considerations as well as fuel storage requirements, there are other ways to pose reasonable design constraints without overconstraining the optimizer. One could enforce a minimum section area for example, or fix the desired thickness only at critical points on the wing.

B. CRM Wing Multimodality Investigation

Earlier work by Osusky et al.[33] suggested that the CRM wing optimization problem as posed is multimodal, having multiple locally optimal solutions. However, difficulties were encountered with converging the optimization, so the solutions obtained may not have been local minima. This question is revisited here,

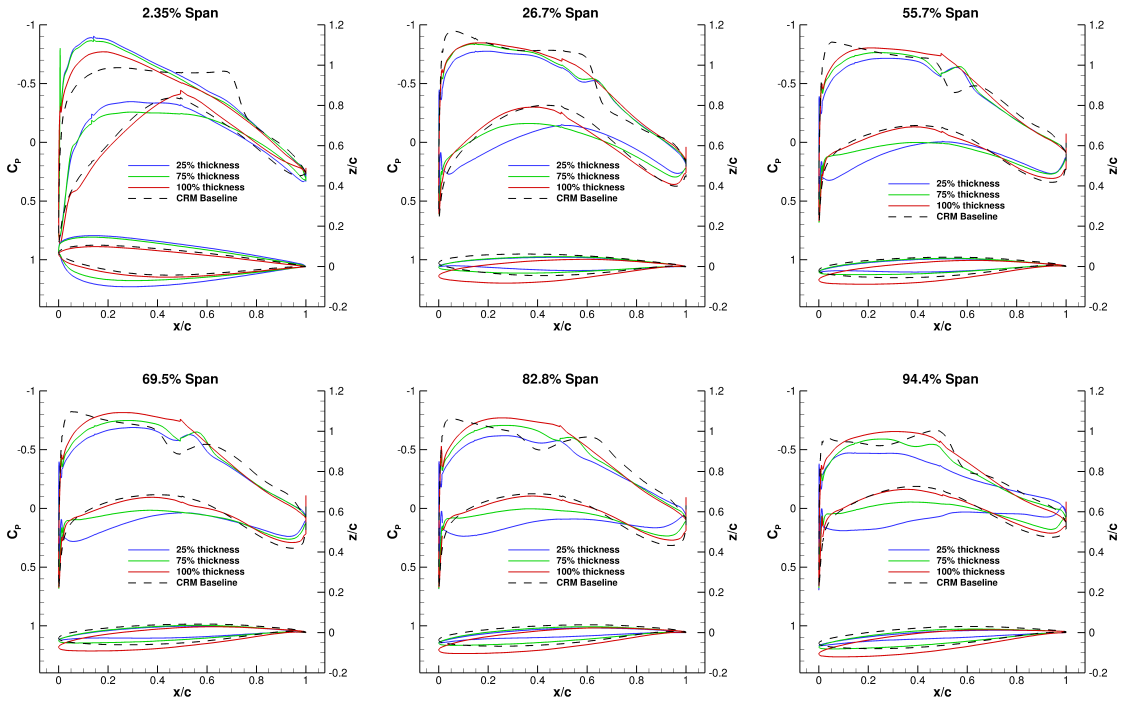

Figure 4: Sectional pressure plots and sections for optimized CRM wings with different thickness constraints, computed on fine mesh

Table 3: Results for CRM wing single-point optimization with different initial geometries, with drag coefficient computed on coarse optimization mesh

	C_D (counts)	C_M
Baseline	218.3	-0.1712
Optimized original geometry	194.5	-0.1700
Optimized with NACA 0012 sections	195.2	-0.1700
Optimized with RAE 2822 sections	195.0	-0.1700
Optimized with SC 20012 sections	195.0	-0.1700
Optimized with SC 20410 sections	194.5	-0.1700

using the 25% minimum thickness constraint. The optimization was run with a number of initial geometries created by replacing the initial geometry of the CRM wing with a specified airfoil section. Each section's chord length and twist are kept constant as in the original CRM wing. This approach results in a much wider variety of starting shapes compared to Osusky et al.,[33] who only applied slight perturbations to the initial wing geometry. The geometric constraints such as volume and thickness are still based on those of the original CRM wing geometry. The airfoils used to create the initial geometries are the NACA 0012, RAE 2822, SC 20012 and SC 20410 sections.[54]

Figure 5 shows the convergence histories for the different optimizations. The feasibility, plotted in Figure 5a, is a measure of how well the nonlinear constraints are satisified. The optimality in Figure 5b, as stated earlier, is a measure of the magnitude of the objective function gradient. The merit function in Figure 5c, is

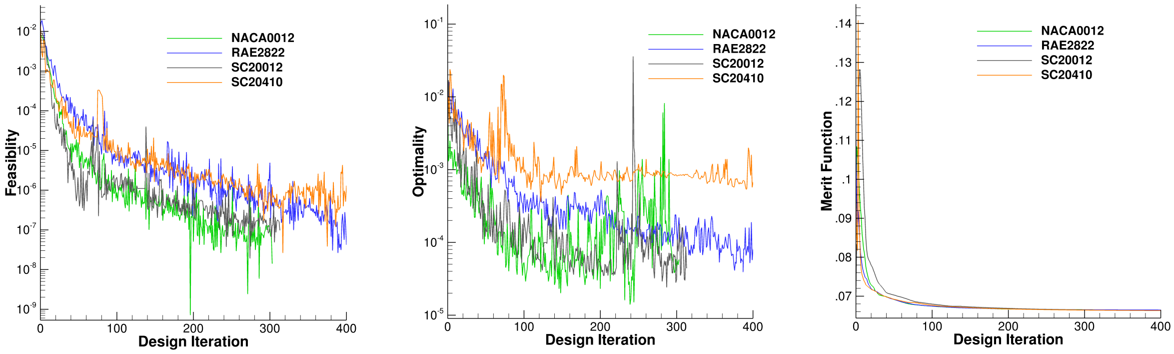

(a) Feasibility

(b) Optimality

(c) Merit Function

Figure 5: Convergence history for the CRM optimization with different initial geometries

the objective function, augmented to include the nonlinear constraint terms. Once the feasibility has been reduced by several orders of magnitude, the value of the merit function becomes the objective function, which in this case is drag.

Each case was run for over 300 iterations until the drag values no longer decreased. Table 3 summarizes the optimized drag coefficients evaluated at $C_L = 0.50$, and Figure 6 shows the optimized sections and pressure distributions. All of the optimized geometries are within one drag count of the original single-point optimization and the section shapes are nearly the same. There is a small glitch in pressure coefficient near the root wing section, caused by curvature mismatches from fitting the original CRM wing with the specified airfoils. Nevertheless, the pressure plots for each of the runs show a strong resemblance to each other. With the exception of the SC 20410 case, all the runs reduced the optimality by two orders of magnitude, which suggests that they are close to the optimum. In Figure 6, the SC 20410 optimization shows some deviation in section shape from the rest of the geometries at 55.7% span. Since this is the also the case with the least optimality reduction, it is likely that this case is simply unconverged as opposed to being a distinct local minimum. The similarities in the section shapes suggest that the CRM wing optimization does not have multiple local optima and is in fact unimodal. While this conclusion contradicts that of Osusky et al.,[33] the improved optimality reductions here make the current results more definitive.

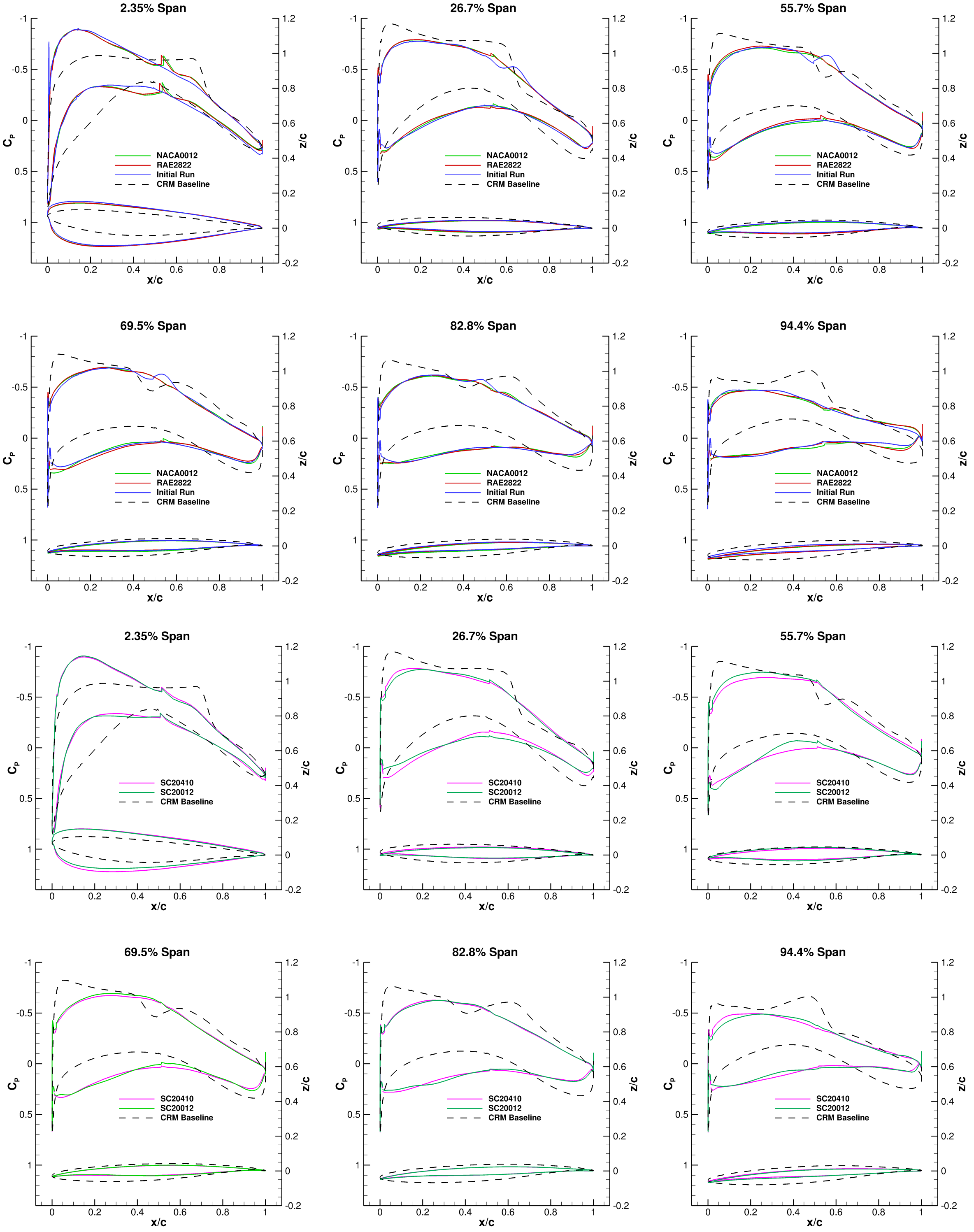

Figure 6: Sectional pressure plots and sections for optimized CRM wings with different initial geometries, computed on the optimization mesh

Table 4: Planform variable limits

Variable	Units	Upper	Lower
Half-Span	ref. units	3.95	1.00
Chord	ref. units	2.0	0.1
Taper	ratio	20.0	0.10
Tip Twist	degrees	4.0	-4.0
Quarter Chord Sweep	degrees	32.0	-32.0
Angle of Attack	degrees	-4.0	4.0

C. Planform and Section Optimization

While optimization problems such as the CRM wing section are useful benchmarks, they involve relatively small changes in the geometry. The next two cases revisit the planform optimization cases studied by Osusky et al.[33] to investigate Jetstream's ability to handle much larger geometric changes. Recognizing that other considerations come into play as well, Jetstream is tasked with minimizing drag on an initially rectangular NACA 0012 wing for transonic flight at two different Mach numbers. The initial chord length is used as the reference unit, and the starting half-span is 3.0 times this length. The design space for these two problems is much larger, with sweep, span, taper, section shape, twist and angle of attack as design variables. The projected area of the wing S is initially equal to 3.0 squared reference units, but since it will change during the optimization, the objective function is specified as the product of the drag coefficient and the non-dimensionalized reference area, $C_D S$, while the lift constraint is specified as $C_L S$. The limits on the planform variables, shown in Table 4, are chosen so that they allow for significant planform change but are somewhat realistic. Nevertheless, this is intended as a problem for testing the methodology, not a practical design study. The wing is optimized at a Reynolds number of 2 million and Mach numbers of 0.78 and 0.85. The following constraints are imposed:

- a lift constraint, $C_L S = 2.0$;
- a minimum thickness-to-chord ratio of 10%, to prevent unusually thin sections;
- a minimum volume constraint, equal to the initial volume, $V = 0.24$ cubed reference units;
- a maximum root bending moment, equal to that of an elliptical lift distribution with a half-span of 4.0 reference units.

In the study performed by Osusky et al.,[33] difficulties with obtaining converged flow solutions and mesh deformation led to poor optimization convergence. To address issues with the flow solver, an O grid topology was used instead of the H grid in the previous work to create higher quality cells near the wing surface. Table 5 lists some of the statistics for the grids used in this study, with the 'Coarse' level being used for

Table 5: Grid parameters for planform optimization

Grid Level	Nodes	Blocks	Off-wall Spacing (ref. units)	Average y^+
Coarse	1,320,000	64	1.35×10^{-6}	0.75
Fine	10,560,000	512	7.30×10^{-7}	0.32

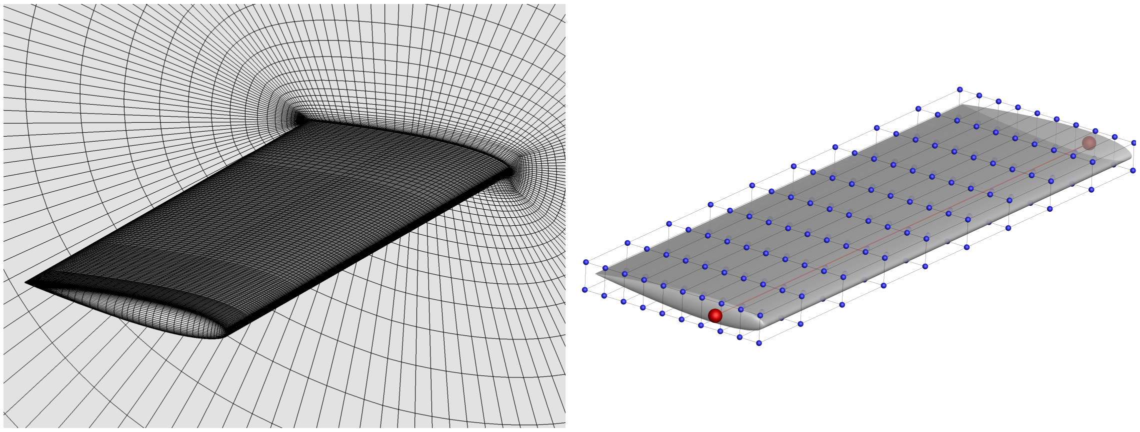

(a) CFD Mesh

(b) FFD Parameterization

Figure 7: CFD Mesh and FFD for the initial rectangular NACA 0012 wing. The wing is controlled by the FFD lattice points (blue) and the axial control points (red)

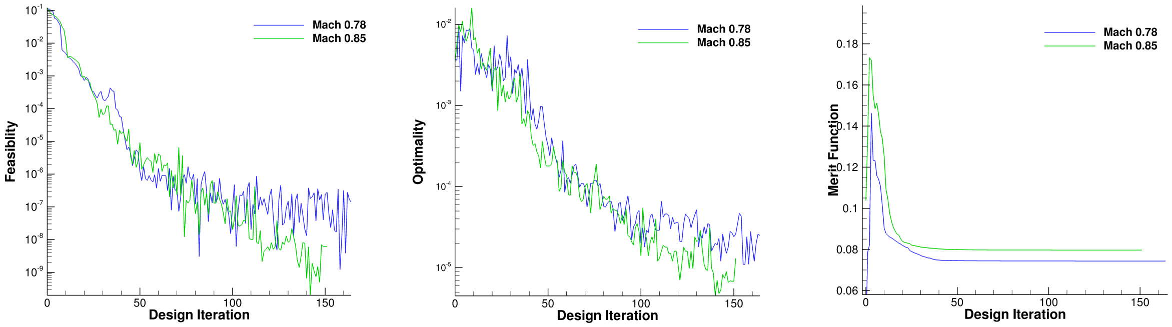

(a) Feasibility

(b) Optimality

(c) Merit Function

Figure 8: Convergence history for the planform and section optimization

optimization. In addition, the axially driven FFD volume approach is used, which allows for more robust manipulation of the wing surface and prevents the creation of intersecting surfaces. Figure 7 shows the computational mesh and the FFD setup for this optimization, with a simple linear axial curve. The axial control point at the root is fixed, while the control point at the tip can translate in order to change the span or sweep.

Results

Figure 8 shows the optimization convergence histories - both optimization cases are able to run without error for over 150 iterations and achieve about three orders of magnitude reduction in optimality. Table 6

Table 6: Results summary for the planform and section optimization

	Mach 0.78		**Mach 0.85**	
	Initial	Optimized	Initial	Optimized
C_L	0.106	0.608	0.0787	0.563
S (ref. units^2)	2.92	3.29	2.92	3.55
$C_L S$	0.31	2.00	0.23	2.00
$C_D S$	0.0302	0.0682	0.0995	0.0727
C_D (counts)	103	207	340	205
L/D	10.3	29.3	2.3	27.5
α	1.0°	3.19°	1.0°	2.83°
Span (ref. units)	2.95	3.95	2.95	3.95
Root Chord (ref. units)	1.00	1.42	1.00	1.36
Taper Ratio	1.00	0.17	1.00	0.32
Sweep Angle	0°	32.0°	0°	32.0°

compares the initial and optimized wings for the Mach 0.78 and Mach 0.85 optimizations. The thickness, volume, and root bending moment constraints are active at convergence in both optimizations. All lift and drag values are computed on the ‘Fine’ mesh level listed in Table 5.

Of the planform variables, only the span and sweep variables are at their upper limit, the former to minimize induced drag and the latter to reduce wave drag. In each case, the taper of the wing is used to optimize both the spanwise loading to reduce induced drag and the wetted surface area to reduce friction drag. At the higher Mach number of 0.85, the optimized planform has a larger wing area to reduce the lift coefficient, reducing wave drag at the cost of increasing friction drag. Figures 9 and 10 show the optimized planform geometries, pressure contours, as well as section data at various spanwise locations. The section shapes show significant change from the initial NACA 0012 airfoil and are all free of strong shocks. The sections optimized for Mach 0.85 have a flatter upper surface and reduced camber compared to the sections optimized at Mach 0.78. The minimum thickness-to-chord ratio constraint is active on the final optimized geometry, preventing the optimizer from creating unusually sharp leading edges as in the CRM optimization. An oscillation in the pressure distribution appears near the tip in Figure 10 in the fine mesh analysis, which was not apparent in the coarse mesh analysis. Running the optimization at a finer mesh level would likely remove this feature. While a more realistic wing design problem would incorporate constraints for low-speed performance or dive conditions, the results of this case are a stiff test of the aerodynamic optimization methodology and its ability to make significant geometric changes.

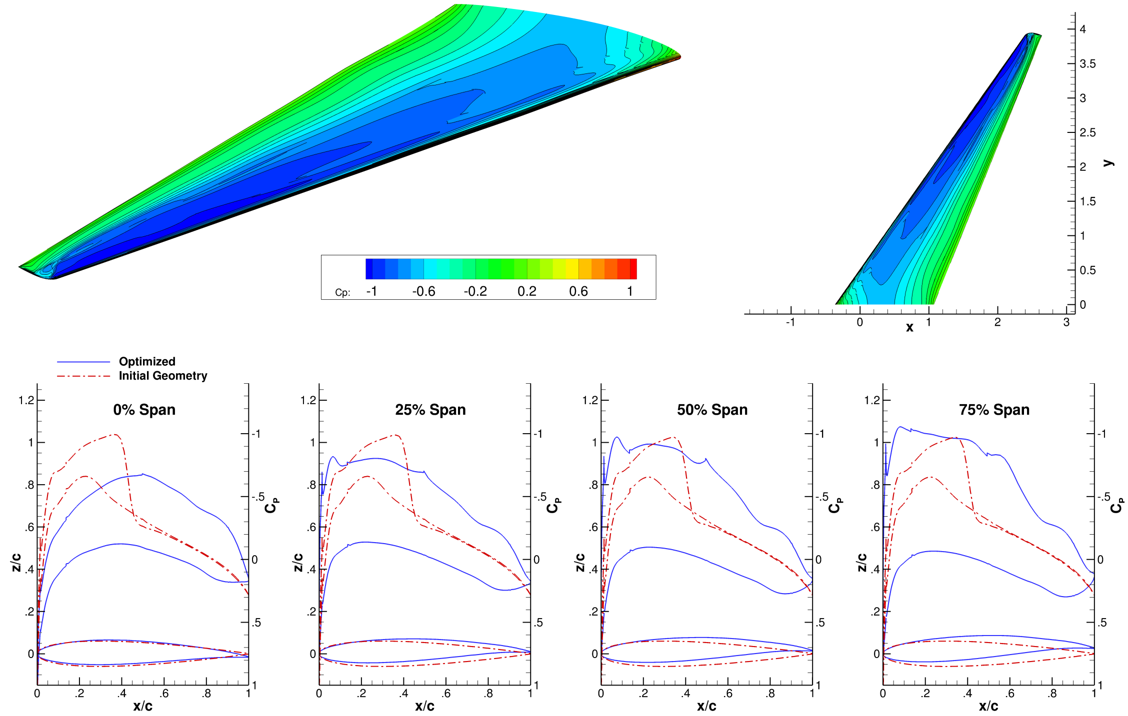

Figure 9: Optimized planform and section geometry and upper surface pressure contours at Mach 0.78, computed on the fine mesh

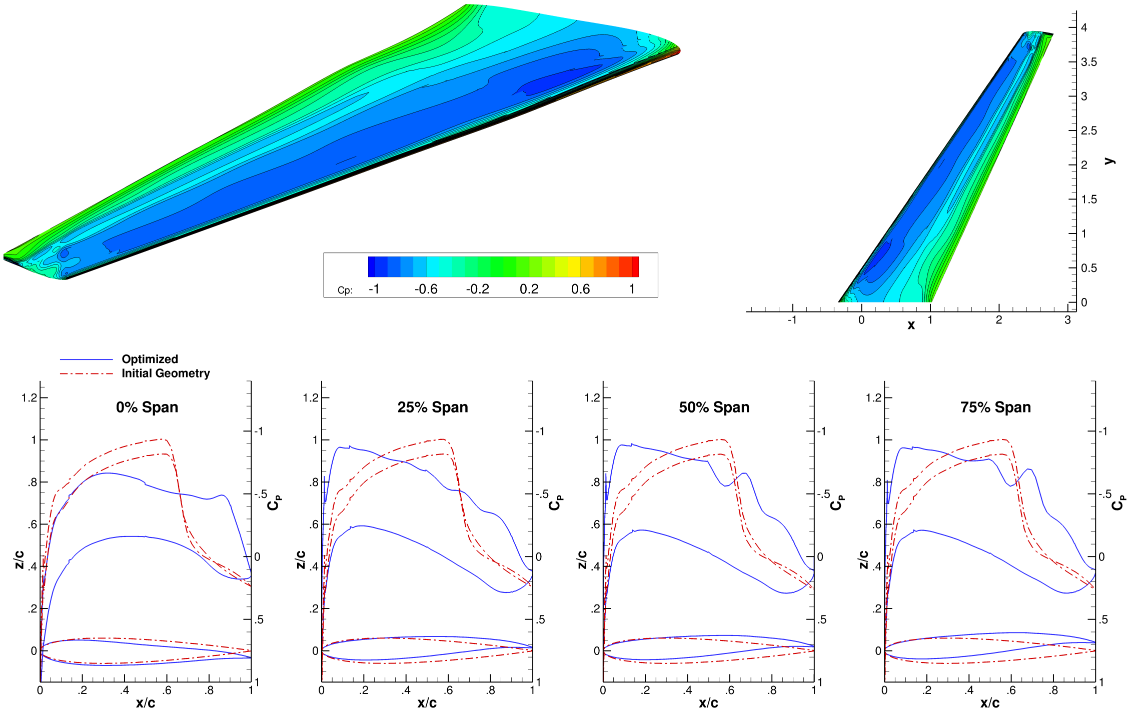

Figure 10: Optimized planform and section geometry and upper surface pressure contours at Mach 0.85, computed on the fine mesh

D. Non-planar Wingtip Optimization

While the previous case involved large planform shape changes, this study examines the performance of the optimizer when the design space includes non-planar geometries. Whereas CFD is typically used to analyze the tradeoffs of various winglet configurations, the goal of this case is to use numerical techniques to design wingtip configurations from a planar geometry, which is quite a stiff test for an optimization methodology. The initial wing geometry has a planform based on the Boeing 737-900, and has untwisted RAE 2822 airfoil sections. The initial geometry and flow conditions are similar to the case studied by Khosravi and Zingg,[55] which was an inviscid aerostructural optimization. Khrosravi and Zingg demonstrated the importance of aerostructural considerations in winglet design, so we emphasize again that the purpose of the present study is to investigate the optimization methodology, not to develop practical wingtip treatments.

For most of the wing, the design variables are the section shape, geometric twist, and the angle of attack. For the last 10% of the wing span, the taper, sweep, and dihedral are design variables in order to design the non-planar wingtip. Since this freedom allows the projected area of the wing to change, the lift constraint is again specified as the product of the reference area and lift coefficient. The wing is optimized at a Reynolds number of 20 million and a Mach number of 0.78. In addition to design variable bounds, the following constraints are imposed:

- a minimum lift constraint, $C_L S = 1.45$;
- a minimum thickness-to-chord ratio of 9% at every section;
- a minimum volume constraint between the root and 90% span, $V = 0.1856$ cubed reference units, which is equal to that of the baseline wing;
- the projected half wing span, $b/2 = 3.85$ reference units, remains constant.

The wing geometry is normalized by using the mean aerodynamic chord (MAC) of 3.96 metres (of the initial wing) as the reference unit, making the initial projected area $S = 2.9$ squared reference units and the lift constraint $C_L = 0.50$. As in the previous case, the objective to be minimized is the product $C_D S$. Note that there is no volume constraint for the wingtip portion; it can grow or shrink as needed as long as the sections satisfy the minimum thickness constraint.

The first row in Table 7 show the grid parameters for the initial B737 wing, which is meshed with an O-grid topology. The mesh is additionally refined in the spanwise direction near the wing tip as the optimizer is expected to bend and deform the wing it. The FFD volume control method is used here, this time with two separate volumes. The first FFD volume governs the majority of the wing from the root to 90% of the span; this portion of the wing can optimize section shape and twist but not the planform. The second FFD

Table 7: Grid parameters for the wingtip optimization study

Initial Geometry	Grid Level	Blocks	Nodes	Off-wall Spacing (ref. units)	Average y^+
B737 with RAE 2822 Sections	Coarse	1,631,000	64	7.8×10^{-7}	0.45
	Fine	13,048,000	512	3.2×10^{-7}	0.23
B737 with Wingtip Fence	Coarse	3,108,336	112	9.8×10^{-7}	0.51
	Fine	13,039,488	896	4.5×10^{-7}	0.24
B737 with Split-tip	Coarse	2,114,448	112	10.4×10^{-7}	0.62
	Fine	16,642,752	448	6.1×10^{-7}	0.31

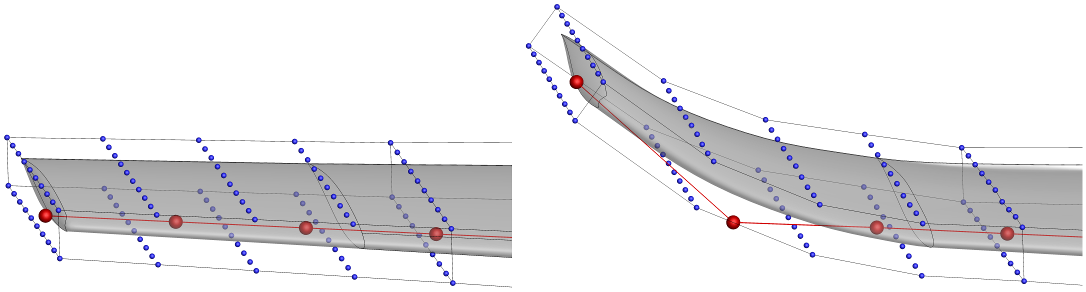

(a) Initially planar wingtip

(b) Wingtip deformed upwards

Figure 11: The FFD control volume near the wingtip, showing how a winglet could be formed. The wing is controlled by the FFD lattice points (blue) and the axial control points (red).

volume, shown in Figure 11, governs the wingtip; in addition to section and twist, the taper is free and the axial curve control points can be allowed to move to adjust sweep and wingtip height. The wingtip axial curve is parameterized with a fourth-order B-spline curve to ensure a smooth blend from the planar wing to the winglet.

Four cases are optimized on this wing, with gradually increasing levels of geometric freedom. In the first case, only the wing section and twist are design variables. In the second case, the raked wingtip, the optimizer also designs the wing section and twist, with the additional freedom to design taper and sweep at the wingtip. In the third and fourth cases, the optimizer has the added freedom to move the outermost axial control point vertically to create a winglet up or down. The second outermost axial control point has some freedom to move in the spanwise direction to control the radius of curvature of the winglet transition. Finally, the axial control points cannot extend the wing past its original projected span. The maximum height-to-span ratio (h/b) allowed for each winglet is 5%.

In addition, two geometries with dual wingtips are optimized, with the grid parameters shown in the last two rows of Table 7. Both geometries have the same planform and RAE 2822 sections as the first baseline wing. While these grids use the O-grid topology and have similar number of nodes, extra blocks are required in order to properly mesh the dual wingtips. The wingtip fence, shown in Figure 12a, has two wingtips - one up and one down. Each extension is governed by an axial FFD volume and is allowed to change taper,

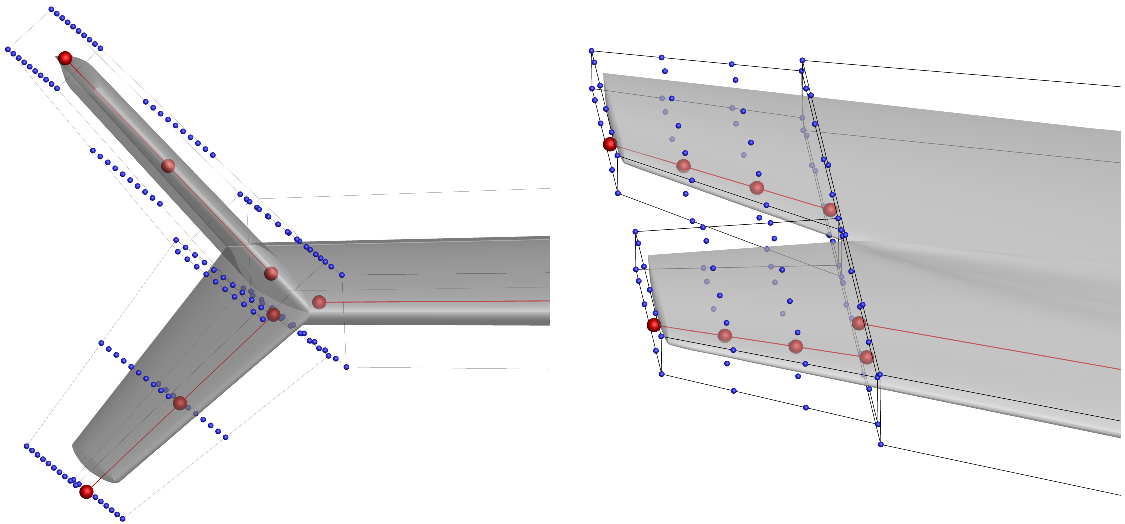

(a) Initial wingtip fence geometry

(b) Initial split-tip geometry

Figure 12: The initial geometry and FFD control volumes for the wingtip fence and split-tip optimizations. The wing is controlled by the FFD lattice points (blue) and the axial control points (red).

sweep, and height independently. The split-tip, shown in Figure 12b, is parameterized similarly, with the wingtips split in the chordwise direction. In both cases, the entire wing section and twist are free, while the total span, volume and lift constraints are kept at the same values as in the above four cases. In addition, the maximum distance between the upper and lower wingtip for both cases is restricted to the same maximum h/b ratio for the winglets.

Results

Table 8 summarizes the optimization results. While the optimizations are performed on the ‘Coarse’ grid level, all of the drag values are computed on the ‘Fine’ grid level shown in Table 7. Although the optimization meshes for the wingtip fence and split-tip are different than the previous four due to their unique topology, the final drag values are computed on a mesh with around 13 million nodes to provide an accurate comparison to the rest of the geometries. Figure 13 shows the initial wing and the wing with optimized section variables. Figures 14 and 15 show the geometries and pressure contours for the wings with optimized wingtips.

In the section-only optimization, the optimizer adjusts the airfoil section and quarter-chord twist to remove the shock and optimize the spanwise lift distribution. In the raked tip, the wingtip is tapered and swept back as far as possible, providing a small improvement. The third case, where the optimizer was given the freedom to move the wingtip vertically in both directions, always resulted in a downward winglet. As a result, the fourth optimization was run with the winglet constrained to move upwards and given a small

Table 8: Results summary for RANS wingtip optimization

	Initial	Section only	Raked Tip	Winglet Down	Winglet Up	Wingtip Fence	Split-tip
$C_L S$	1.450	1.450	1.450	1.450	1.450	1.450	1.450
$C_D S$	0.0497	0.0449	0.0445	0.0435	0.0440	0.0438	0.0451
$\Delta C_D S$	0.0%	-9.7%	-10.4%	-12.5%	-11.5%	-11.8%	-9.3%
S	2.899	2.899	2.848	2.874	2.880	2.889	2.885
C_L	0.500	0.500	0.509	0.504	0.503	0.502	0.502
C_D (counts)	171.5	154.9	156.4	151.4	152.8	151.7	156.4
L/D	29.15	32.25	32.53	33.29	32.89	33.05	32.09
α	2.41°	1.44°	1.57°	1.96°	1.83°	1.98°	1.05°
S_{wet}	2.962	2.961	2.906	2.984	2.987	3.026	2.969
$C_{D,\text{pressure}}$	119.6	101.9	103.4	97.5	98.7	96.8	102.2
$C_{D,\text{friction}}$	51.9	53.0	52.9	53.9	54.1	54.9	54.2

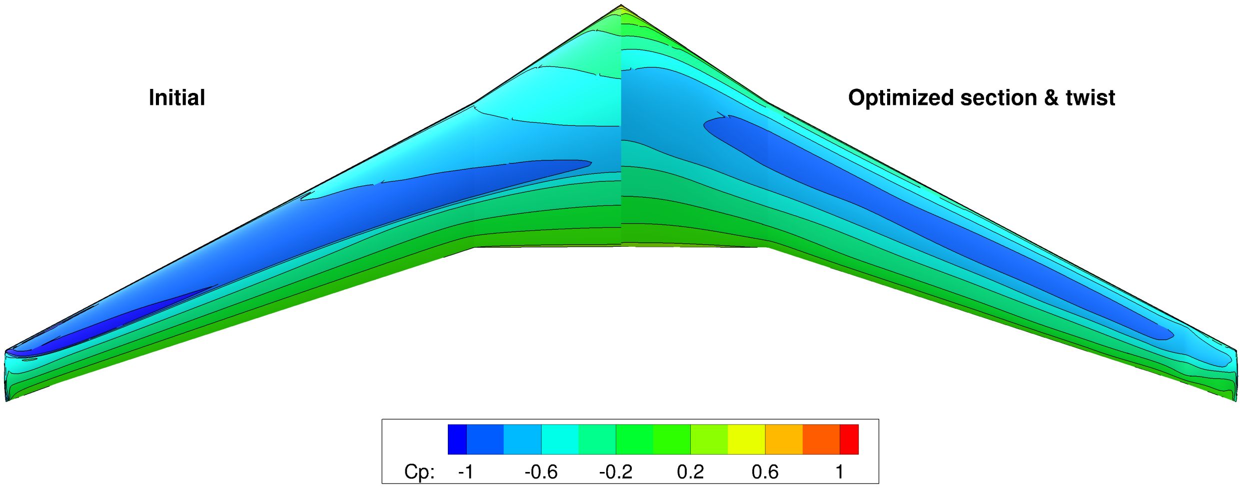

Figure 13: Initial and optimized upper surface pressure contours with no wingtip optimization

initial upward deflection. Under these conditions, the optimizer produced a fully deflected upward winglet, suggesting that this is a local optimum for this problem.

The optimized winglet down leads to the greatest improvement in drag. In both the winglet up and down configurations, the optimizer designs the winglet to reach the maximum h/b, while increasing the wetted area. The drag breakdown in Table 8 shows that the optimizer is trading off between induced drag and surface friction drag. Both winglets are swept back as far as possible; the winglet down has washout while the winglet up has wash-in. Finally, both winglets are tapered to decrease the projected area.

The wingtip fence shows a significant improvement in drag compared to the initial geometry, despite having the greatest wetted area. An interesting feature in this case is that the downward facing tip is

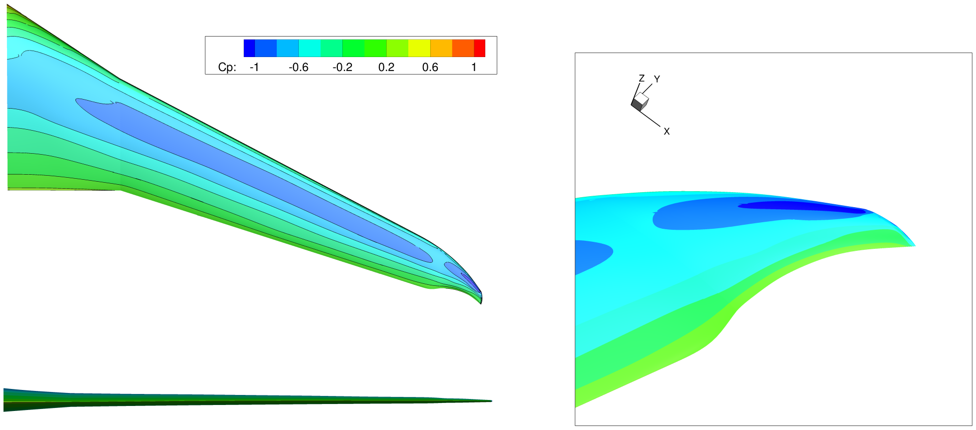

(a) Optimized raked wingtip

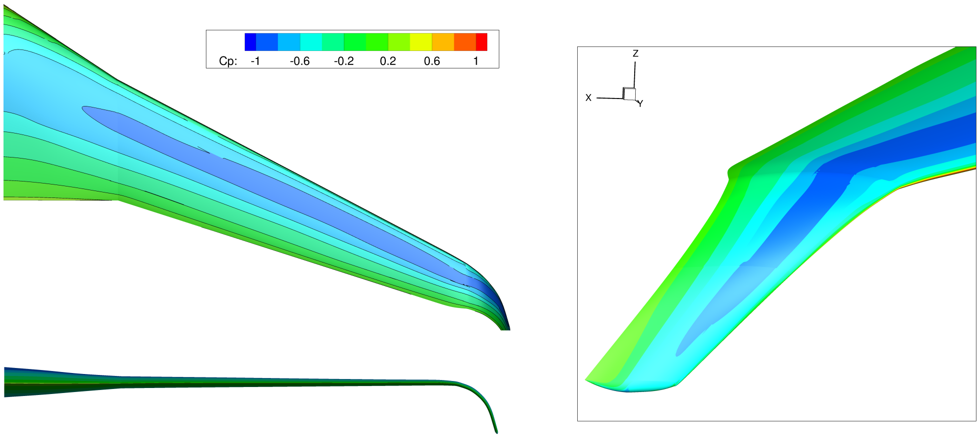

(b) Optimized winglet down

Figure 14: Optimized geometries and upper surface pressure contours for raked and winglet down configurations

tapered less and has greater area than the upward tip. While both wingtips are initially level in the split-tip, the optimizer moves the forward tip upward and the aft tip downward. This is a similar result to that of Hicken and Zingg,[30] who studied a similar geometry with an earlier iteration of Jetstream in inviscid subsonic flow. In the optimized wingtip fence and split-tip geometries, the downward wingtip has wash-out and the upward wingtip has wash-in. While the optimized split-tip geometry bears some resemblance to the wingtip fence, it appears to have a higher drag due to the geometry at the junction at the two tips, which presented some difficulty for the flow solver. We also note that further turbulence model validation is needed to ensure that the solver produces accurate results in the junction regions. Finally, while the all of the optimized geometries are mostly shock-free, small shocks can be seen on the wing tips of the winglet up and split-tip geometries. This is most likely caused by having too few section design variables at the wingtip, shown in Figure 12, and can be addressed by giving the optimizer more freedom in that area.

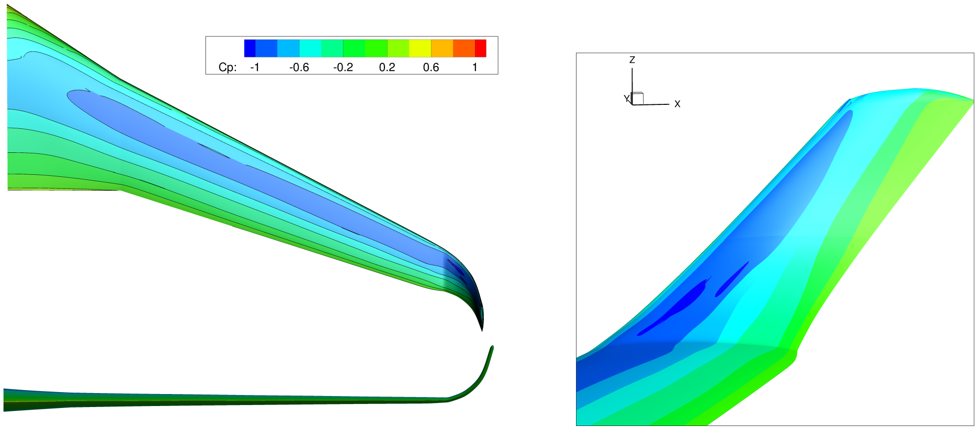

(a) Optimized winglet up

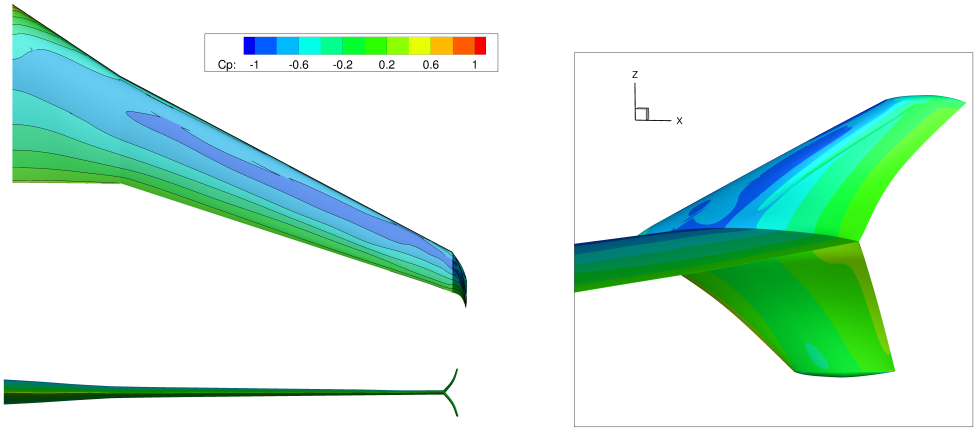

(b) Optimized wingtip fence

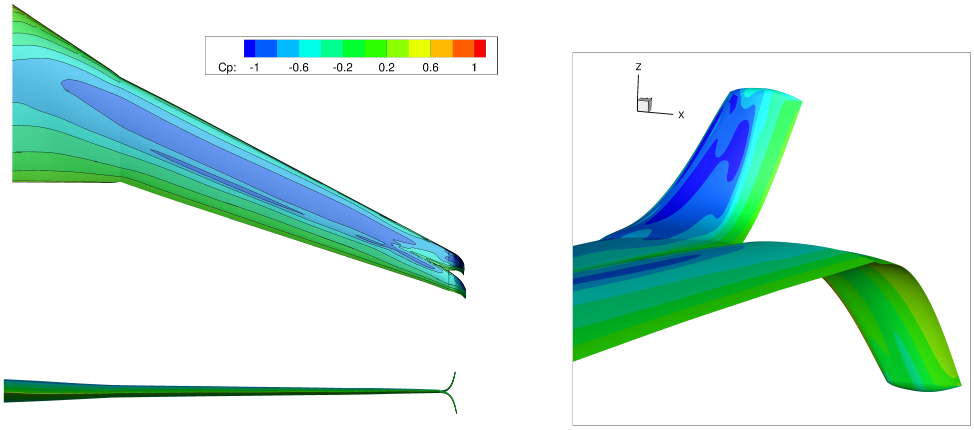

(c) Optimized split-tip

Figure 15: Optimized geometries and upper surface pressure contours for winglet up, wingtip fence and split-tip configurations

IV. Conclusions

The results of the optimization problems presented in this paper demonstrate the capabilities of a Newton-Krylov aerodynamic shape optimization methodology based on flows governed by the RANS equations. The CRM wing optimization was revisited with a focus on characterizing the design space of the CRM wing benchmark optimization with respect to varying thickness constraints. Furthermore, optimization runs starting from various user-generated initial geometries suggest that the design space of the CRM wing optimization is likely not multimodal.

The last two cases demonstrate the ability of the methodology used by Jetstream to handle successfully optimization problems involving large geometric changes. Starting from a rectangular wing with NACA 0012 sections, the optimizer is able to optimize both the planform and wing section to develop a typical wing geometry for transonic conditions. Finally, the study of wing-tip devices on the B737-900 geometry demonstrates that it is possible to apply a RANS-based optimization methodology to the design of complex, non-planar geometries.

Acknowledgements

The authors gratefully acknowledge the financial assistance from the National Sciences and Engineering Research Council, the Ontario Graduate Scholarship program, and the University of Toronto. Computations were performed on the GPC supercomputer at the SciNet HPC Consortium, part of Compute Canada. SciNet is funded by: the Canada Foundation for Innovation under the auspices of Compute Canada, the Government of Ontario, Ontario Research Fund - Research Excellence, and the University of Toronto.

References

[1]IATA, "IATA Annual Review 2014," 2014.

[2]IATA, "IATA Annual Review 2013," 2013.

[3]Pironneau, O., "On Optimum Design in Fluid Mechanics," *Journal of Fluid Mechanics*, Vol. 64, No. 1, 1974, pp. 97–110.

[4]Angrand, F., "Optimum Design for Potential Flows," *International Journal for Numerical Methods in Fluids*, Vol. 3, 1983, pp. 265–282.

[5]Jameson, A., "Aerodynamic Design via Control Theory," *Journal of Scientific Computing*, Vol. 3, No. 3, 1988, pp. 233–260.

[6]Zingg, D. W., Nemec, M., and Pulliam, T. H., "A Comparative Evaluation of Genetic and Gradient-Based Algorithms applied to Aerodynamic Optimization," *European Journal of Computational Mechanics, REMN*, Vol. 17, 2008, pp. 103–126.

[7]Jameson, A. and Reuther, J., "Control Theory based Airfoil Design using Euler Equations," *5th Symposium on Multidisciplinary Analysis and Optimization*, No. AIAA 1994-4272, September 1994.

[8]Anderson, W. K. and Bonhaus, D. L., "Airfoil Design on Unstructured Grids for Turbulent Flows," *AIAA Journal*, Vol. 37, No. 2, 1999, pp. 185–191.

[9]Nemec, M., Zingg, D. W., and Pulliam, T. H., "Multipoint and Multi-Objective Aerodynamic Shape Optimization," *AIAA Journal*, Vol. 42, No. 6, June 2004, pp. 1057–1065.

[10]Elliot, J. and Peraire, J., "Practical 3D Aerodynamic Design and Optimization using Unstructured Meshes," *AIAA Journal*, Vol. 35, No. 9, September 1997.

[11]Nielsen, E. J. and Anderson, W. K., "Aerodynamic Optimization on Unstructured Meshes using the Navier-Stokes equations," *AIAA Journal*, Vol. 37, No. 11, November 1999, pp. 1411–1419.

[12]Jameson, A., Pierce, N., and Martinelli, L., "Optimum Aerodynamic Design using the Navier-Stokes equations," *Theoretical and Computational Fluid Dynamics*, Vol. 10, 1998, pp. 213–237.

[13]Meheut, M., Destarac, D., Carrier, G., Anderson, G., Nadarajah, S., Poole, D., Vassberg, J., and Zingg, D. W., "Gradient-Based Single and Multi-point Aerodynamic Optimizations with the elsA Software," *53rd AIAA Aerospace Sciences Meeting*, No. AIAA 2015-0263, Kissimmee, Florida, January 2015.

[14]Peigin, S. and Epstein, B., "Robust Drag Minimization of Aerodynamic Wings in Engineering Environment," *Journal of Aircraft*, Vol. 43, 2006, pp. 1195–1203.

[15]Epstein, B., Jameson, A., Peigin, S., Roman, D., Harrison, N., and Vassberg, J., "Comparative Study of 3D Wing Drag Minimization by Different Optimization Techniques," *46th AIAA Aerospace Sciences Meeting*, No. AIAA-2008-326, Reno, Nevada, U.S.A., January 2008.

[16]Ledoux, S. T., Young, D. P., Fugal, S., Elliot, J., Huffman, W. P., and Melvin, R. G., "An Updated Study for the AIAA Aerodynamic Design Optimization Design Group Test Case-4," *AIAA Science and Technology Forum and Exposition 2014: 53rd Aerospace Sciences Meeting*, No. AIAA 2015-1717, Kissimmee, Florida, January 2015.

[17]Chen, S., Lyu, Z., Kenway, G. K. W., and Martins, J. R. R. A., "Aerodynamic Shape Optimization of the Common Research Model Wing-Body-Tail Configuration," *53rd AIAA Aerospace Sciences Meeting*, No. AIAA 2015-1718, Kissimmee, Florida, January 2015.

[18]Anderson, G. R., Nemec, M., and Aftosmis, M. J., "Aerodynamic Shape Optimization Benchmarks with Error Control and Automatic Parameterization," *53rd AIAA Aerospace Sciences Meeting*, No. AIAA 2015-1719, Kissimmee, Florida, January 2015.

[19]Gariepy, M., Malouin, B., Tribes, C., and Trepanier, J. Y., "Direct Search Airfoil Optimization Using Far-Field Drag Decomposition Results," *53rd AIAA Aerospace Sciences Meeting*, No. AIAA 2015-1720, Kissimmee, Florida, January 2015.

[20]Iuliano, E. and Quagliarella, D., "Evolutionary Optimization of Benchmark Aerodynamic Cases using Physics-based Surrogate Models," *53rd AIAA Aerospace Sciences Meeting*, No. AIAA 2015-1721, Kissimmee, Florida, January 2015.

[21]Fusi, F., Quaranta, G., Guardone, A., and Congedo, P. M., "Drag Minimization of an Isolated Airfoil in Transonic Inviscid Flow by Means of Genetic Algorithms," *53rd AIAA Aerospace Sciences Meeting*, No. AIAA 2015-1722, Kissimmee, Florida, January 2015.

[22]Masters, D. A., Taylor, N. J., Rendall, T. C. S., Allen, C. B., and Poole, D. J., "Geometric Comparison of Aerofoil Shape Parameterization Methods," *AIAA Journal*, 2017, doi:10.2514/1.J054943.

[23]Ledoux, S. T., Vassberg, J. C., Young, D. P., Fugal, S., Kamenetskiy, D., Huffman, W. P., Melvin, R. G., and Smith, M. F., "Study based on the AIAA Aerodynamic Design Optimization Discussion Group Test Cases," *AIAA Journal*, Vol. 53, No. 7, July 2015, pp. 1910–1935.

[24]Reist, T. A. and Zingg, D. W., "High-Fidelity Aerodynamic Shape Optimization of a Lifting-Fuselage Concept for Regional Aircraft," accepted by Journal of Aircraft, 2016. doi:10.2514/1.C033798.

[25]Gagnon, H. and Zingg, D. W., "Euler-Equation-Based Drag Minimization of Unconventional Aircraft Configurations," *Journal of Aircraft*, Vol. 53, No. 5, September 2016, pp. 1361–1371.

[26]Drela, M., "Development of the D8 Transport Configuration," *29th AIAA Applied Aerodynamics Conference*, No. AIAA 2011-3970, Honolulu, Hawaii, June 2011.

[27]Jansen, P. W., Perez, R. E., and Martins, J. R. R. A., "Aerostructural Optimization of Nonplanar Lifting Surfaces," *Journal of Aircraft*, Vol. 47, No. 5, September-October 2010, pp. 1490–1503.

[28]Ning, S. A. and Kroo, I., "Multidisciplinary Considerations in the Design of Wings and Wing Tip Devices," *Journal of Aircraft*, Vol. 47, No. 2, March-April 2010, pp. 534–543.

[29]Hicken, J. E. and Zingg, D. W., "Aerodynamic Optimization with Integrated Geometry Parameterization and Mesh Movement," *AIAA Journal*, Vol. 48, No. 2, February 2010, pp. 401–413.

[30]Hicken, J. E. and Zingg, D. W., "Induced-Drag Minimization of Nonplanar Geometries based on the Euler Equations," *AIAA Journal*, Vol. 48, No. 11, November 2010, pp. 2564–2575.

[31]Aly, S., Ogot, M., and Peliz, R., "Stochastic Approach to Optimal Aerodynamic Shape Design," *Journal of Aircraft*, Vol. 33, No. 5, 1996, pp. 956–961.

[32]Chernukhin, O. and Zingg, D. W., "Multimodality and Global Optimization in Aerodynamic Design," *AIAA Journal*, Vol. 51, No. 6, 2013, pp. 1342–1354.

[33]Osusky, L., Buckley, H. P., Reist, T. A., and Zingg, D. W., "Drag Minimization based on the Navier-Stokes Equations Using a Newton-Krylov approach," *AIAA Journal*, Vol. 53, No. 6, June 2015, pp. 1555–1577.

[34]Yu, T. Y. and Soni, B. K., "Application of NURBS in Structured Grid Generation," *Computer-Aided Design*, Vol. 27, 1995, pp. 147–157.

[35]Truong, A. H., Oldfield, C. A., and Zingg, D. W., "Mesh Movement for a Discrete-Adjoint Newton-Krylov Algorithm for Aerodynamic Optimization," *AIAA Journal*, Vol. 46, No. 7, 2008, pp. 1695–1704.

[36]Meijerink, J. A. and Vorst, H. A. V. D., "An Iterative Solution Method for Linear Systems of which the coefficient Matrix is a symmetric M-Matrix," *Mathematics of Computation*, Vol. 31, 1977, pp. 148–162.

[37]Anderson, W. K., Karman, S. L., and Burdyshaw, C., "Geometry Parameterization Method for Multidisciplinary Applications," *AIAA Journal*, Vol. 47, No. 6, June 2009, pp. 1568–1578.

[38] Gagnon, H. and Zingg, D., "Two-level Free-Form and Axial Deformation for Exploratory Aerodynamic Shape Optimization," *AIAA Journal*, Vol. 53, No. 7, July 2015, pp. 2015–2026.

[39] Osusky, M. and Zingg, D. W., "A Parallel Newton-Krylov-Schur Flow Solver for the Reynolds-averaged Navier-Stokes Equations discretized using summation-by-parts operators," *AIAA Journal*, Vol. 51, No. 12, December 2013, pp. 2833–2851.

[40] Fernandez, D. C. D. R., Hicken, J. E., and Zingg, D. W., "Review of Summation-By-Parts Operators with Simultaneous Approximation Terms for the Numerical Solution of Partial Differential Equations," *Computers and Fluids*, Vol. 95, 2014, pp. 171–196.

[41] Jameson, A., Schmidt, W., and Turkel, E., "Numerical Solutions of the Euler Equations by Finite Volume Methods using Runge-Kutta Time-Stepping Schemes," *14th Fluid and Plasma Dynamics Conference*, No. AIAA-81-1259, Palo Alto, California, 1981.

[42] Pulliam, T. H., "Numerical Techniques for Viscous Flow Computation in Turbomachinery Bladings," Tech. rep., The von Kármán Inst. for Fluid Dynamics, Rhode-Saint-Genèse, Belgium, 1986.

[43] Swanson, R. C. and Turkel, E., "On Central-Difference and Upwind Schemes," *Journal of Computational Physics*, Vol. 101, No. 2, 1992, pp. 292–306.

[44] Osusky, M., Boom, P., and Zingg, D. W., "Results from the Fifth AIAA Drag Prediction Workshop Obtained with a Parallel Newton-Krylov-Schur Flow Solver Discretized using Summation-by-Parts Operators," No. AIAA-2013-2511, San Diego, CA, June 2013.

[45] Gunzburger, M., "Introduction to the Mathematical Aspects of Flow Control and Optimisation," Tech. rep., The von Kármán Inst. for Fluid Dynamics, Rhode-Saint-Genèse, Belgium, 1997.

[46] Hicken, J. E. and Zingg, D. W., "A Simplified and Flexible Variant of GCROT for Solving Nonsymmetric Linear Systems," *SIAM Journal on Scientific Computing*, Vol. 32, No. 3, June 2010, pp. 1672–1694.

[47] Gill, P., Murray, W., and Saunders, M. A., "SNOPT: An SQP Algorithm for Large-Scale Constrained Optimization," *SIAM Review*, Vol. 47, 2005, pp. 99–131.

[48] Lee, C., Koo, D., and Zingg, D. W., "Comparison of B-spline Surface and Free-Form Deformation Geometry Control for Aerodynamic Optimization," *AIAA Journal*, Vol. 55, No. 1, 2017, pp. 228–240.

[49] Lee, C., Koo, D., Telidetzki, K., Buckley, H., and Zingg, D. W., "Aerodynamic Shape Optimization of Benchmark Problems using Jetstream," *AIAA Science and Technology Forum and Exposition 2014: 53rd Aerospace Sciences Meeting*, No. AIAA 2015-0262, Kissimeee, Florida, January 2015.

[50] Lyu, Z., Kenway, G. K. W., and Martins, J. R. R. A., "Aerodynamic Shape Optimization Investigations of the Common Research Model Wing Benchmark," *AIAA Science and Technology Forum and Exposition*, No. AIAA-2014-0567, National Harbor, Maryland, January 2014.

[51] Amoignon, O., Navratil, J., and Hradil, J., "Study of Parameterizations in the Project CEDESA," *AIAA Science and Technology Forum and Exposition*, No. AIAA-2014-0570, National Harbor, Maryland, January 2014.

[52] Epstein, B., Peigin, S., Bolsunovsky, A., and Timchenko, S., "Aerodynamic Shape Optimization by Automatic Hybrid Genetic Tool OPTIMENGA AERO," *AIAA Science and Technology Forum and Exposition*, No. AIAA-2014-0569, National Harbor, Maryland, January 2014.

[53] Carrier, G., Destarac, D., Dumont, A., Meheut, M., Salah-El-Din, I., Peter, J., and Khelil, S. B., "Gradient-Based Aerodynamic Optimization with the elsA Software," *AIAA Science and Technology Forum and Exposition*, No. AIAA-2014-0568, National Harbor, Maryland, January 2014.

[54] Harris, C. D., "NASA Supercritical Airfoils: A Matrix of Family-Related Airfoils," Tech. Rep. 2969, NASA, 1990.

[55] Khosravi, S. and Zingg, D. W., "Aerostructural Perspective on Winglets," accepted by Journal of Aircraft, 2017.